ChemPubSoc Europe

DOI: 10.1002/cctc.201402925

CHEMCATCHEM Communications

Assessment of the 3D Pore Structure and Individual Components of Preshaped Catalyst Bodies by X-Ray Imaging

Julio C. da Silva,*[a] Kevin Mader,[a] Mirko Holler,[a] David Haberthür,[a] Ana Diaz,[a] Manuel Guizar-Sicairos,[a] Wu-Cheng Cheng,[b] Yuying Shu,[b] Jörg Raabe,[a] Andreas Menzel,[a] and Jeroen A. van Bokhoven*[a, c]

Porosity in catalyst particles is essential because it enables reactants to reach the active sites and it enables products to leave the catalyst. The engineering of composite-particle catalysts through the tuning of pore-size distribution and connectivity is hampered by the inability to visualize structure and porosity at critical-length scales. Herein, it is shown that the combination of phase-contrast X-ray microtomography and high-resolution ptychographic X-ray tomography allows the visualization and characterization of the interparticle pores at micro- and nanometer-length scales. Furthermore, individual components in preshaped catalyst bodies used in fluid catalytic cracking, one of the most used catalysts, could be visualized and identified. The distribution of pore sizes, as well as enclosed pores, which cannot be probed by traditional methods, such as nitrogen physisorption and isotherm analysis, were determined.

Fluid catalytic cracking (FCC) is the most important conversion process in the refinery, upgrading the heavy fraction of oil into gasoline and volatile olefins.[1] The catalyst bodies are spheres made of various components with a diameter of approximately 100 microns. Reactants must diffuse into and through the preshaped catalyst body to reach an active site. Because large molecules must react on the surface of the catalytic particles that are encompassed in the preshaped catalyst bodies, these bodies contain a large fraction of interparticle space. Thus, the size and connectivity of the pores created by the interparticle space and the relative orientation of the various components within the preshaped particle play an important role in catalysis.

The main FCC catalytic component is a steamed zeolite, H-USY, and other components include alumina, silica–alumina, and clays.[2] Zeolites are crystalline alumina silicates that contain Brønsted acid sites.[2] Although this microporous material[3] is already widely used in the refinery, mesoporous materials are also of interest for catalysis because mesopores in the FCC catalyst improve the diffusion of large molecules into the catalyst bodies, thus enhancing catalytic performance. Indeed, mesostructured zeolites type Y with excellent hydrothermal stability have been demonstrated, and the mesopores in individual zeolite crystals have been visualized by electron tomography.[4,5]

Nitrogen physisorption, often complemented by mercury porosimetry, and isotherm analysis are the most generally applied characterization methods to study porosity in heterogeneous catalysts.[6–8] Adsorption of molecules of a particular size provides direct insight into the accessibility of the interior of crystals and the pore-size openings. Although these methods are widely applied to probe large sample volumes, they yield only averaged parameters, and the information of individual particles is not accessible. On the other hand, electron microscopy (EM) enables detection and analysis of individual catalyst particles. In the case of the FCC zeolite catalyst, electron tomography has provided insight into the pore structure within the individual zeolite crystals.[9,10] Such visualization of pore size and connectivity stimulated the design of new and optimized trimodal pore structures.[3] Recently, the morphology of commercial spent equilibrium fluid catalytic-cracking catalyst (ECAT) was characterized by X-ray tomography and the distribution of zeolites Y in the catalyst particles was inferred from X-ray fluorescence results.[11] Although the structural variation between individual particles was previously observed,[12,13] as well as pore sizes of approximately 100 nm,[11] the distribution of the different components and the interparticle porosity within a single FCC catalyst body have not been quantified.

Herein, we employ state-of-the-art synchrotron X-ray imaging techniques to analyze the size and connectivity of the 3D pore structure in individual FCC catalyst bodies, as well as the padding of their components. We investigate an FCC composite-catalyst body formed by 5% La_2O_3-exchanged zeolite type Y and metakaolin, which is a calcined kaolin clay consisting of aluminum silicate. In FCC catalysts, the clay is a diluent used to control the level of cracking activity and the rare-earth-exchanged zeolites are used to improve hydrothermal stability.

[a] Dr. J. C. da Silva, Dr. K. Mader, Dr. M. Holler, Dr. D. Haberthür, Dr. A. Diaz, Dr. M. Guizar-Sicairos, Dr. J. Raabe, Dr. A. Menzel, Prof. Dr. J. A. van Bokhoven
Paul Scherrer Institut, Villigen PSI, 5232 (Switzerland)
E-mail: julio-cesar.da-silva@psi.ch

[b] Dr. W.-C. Cheng, Dr. Y. Shu
Grace Catalysts Technologies, 7500 Grace Drive
Columbia, MD 21044 (USA)

[c] Prof. Dr. J. A. van Bokhoven
Institute for Chemical and Bioengineering, ETH Zurich
Zurich, 8093 (Switzerland)
E-mail: jeroen.vanbokhoven@chem.ethz.ch

Supporting information for this article is available on the WWW under http://dx.doi.org/10.1002/cctc.201402925.

This catalyst body was imaged by two X-ray imaging techniques covering two length scales: propagation-based phase-contrast microtomography[14–16] and ptychographic nanotomography.[17–19] The former is a full-field imaging technique, whereas the latter is a scanning coherent diffractive imaging technique. In X-ray ptychography, coherent diffraction patterns are generated by using a spatially confined illumination, which is scanned across the sample such that there is sufficient overlap of adjacent spots illumination footprint. From these patterns, the complex transmittance of the specimen is obtained.[17,20] The technique features high resolving power and high sensitivity and, by combination with computed tomography, provides quantitative 3D density maps of the specimens on the nanoscale.[17–19] In addition, scanning electron microscopy was performed, and some images are shown in Figure SI-1 in the Supporting Information.

For the phase-contrast microtomography experiments, a powder containing the spherical catalyst bodies was added to a quartz capillary with a diameter of 500 μm. A volume of 844.8×844.8×712.8 μm^3 was imaged with 1501 projections. Paganin's phase retrieval approach[15] was applied prior to the tomographic reconstruction. The resulting 3D images with voxel size of 0.33 μm and spatial resolution of approximately 0.7 μm allowed us to probe macropores larger than 700 nm in the inner structure of the catalyst bodies. Figure 1 shows a 3D view of the tomogram of the sample. A cropped volume rendering

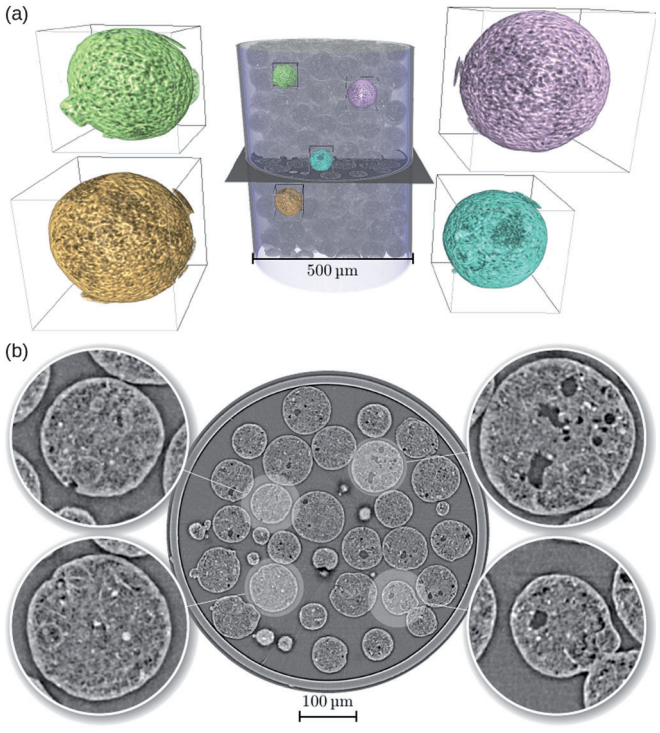

Figure 1. Phase-contrast X-ray microtomography results from the experiment with the FCC catalyst body. a) 3D rendering of the catalyst bodies inside the capillary. Four selected regions of interest of approximately 91×91×91 μm^3 each are marked with different colors and are shown magnified (5×) adjacent to the tomographic volume. b) One axial slice in the middle (shown in (a) for reference) of the phase-contrast tomogram of the sample. Insets show zoomed-in images (3× magnification) of four selected catalyst bodies.

of the capillary with the catalyst bodies inside and some highlighted regions are shown in Figure 1a. An axial slice of the tomogram and four selected particles are highlighted and magnified in the insets of Figure 1b. It was noticed that some pores of a few microns in size are visible, but the smaller pores are barely distinguishable owing to the limited spatial resolution. It was also noticed that a thin shell close to the border of the particles contains fewer pores than the inner part.

To probe those small pores, we needed to obtain 3D images of the same samples with higher resolution. Thus, ptychographic X-ray nanotomography experiments were performed. Unfortunately, the field of view is decreased, but the resolution and sensitivity are enhanced. For this experiment, a pillar of 8 μm diameter was prepared from a spherical catalyst body of the sample by focused ion-beam milling and was mounted on the sample holder of the instrument as described elsewhere.[21,22] 450 ptychographic projections were acquired. Each projection comprised a field of view of 13×11 μm^2 (horizontal×vertical) and was obtained from 419 diffraction patterns. For the ptychographic reconstructions, we used the difference map algorithm,[23] followed by numerical optimization.[24,25] From these projections, a 3D volume was reconstructed by using computed tomography, in which the phase contrast was exploited to obtain high-resolution 3D maps of electron density.[18] The reconstructed 3D images encompass a volume of 12×12×11 μm^3, with a voxel size of 14.3 nm and a spatial resolution of 39 nm. Figure 2a shows a vertical slice of the electron-density tomogram. Two material phases can be clearly distinguished: The 5% La_2O_3-exchanged zeolite type Y and the metakaolin clay. The upper and some lateral parts that appear brighter on the images indicate redeposition of materials during the focused ion-beam (FIB) milling of the sample and are not relevant for our analysis. Some selected axial sections for different vertical positions of the phase-contrast tomograms are shown in Figure 2b, as indicated by the colored squares at the top-left corner of each slice corresponding to the positions of the colored lines in Figure 2a. From Figure 2b, we notice that the region close to the top is filled mostly by the metakaolin clay with a few regions of zeolite agglomerates. In addition, the metakaolin presents squared shapes, whereas zeolites are round and porous, and the interparticle pores have different and irregular shapes with sharp corners.

The mass density of each catalyst component was obtained from the quantitative phase-contrast 3D images obtained with ptychographic X-ray nanotomography.[19] We estimated a mass density of 2.3±0.1 g cm^{-3} for the metakaolin clay and 1.6±0.1 g cm^{-3} for the 5% La_2O_3-exchanged zeolite type Y. Because the exact chemical composition of each of these components is unknown, the ratio of molar mass and the number of electrons of the material was approximated to 2 for the mass density estimate.[26–28] The 3D rendering of all the components identified in this sample is shown in Figure 2c. For the sake of perspicuity, this 3D rendering was made out of a smaller cylinder of 6 μm radius extracted from the sample tomogram during the image segmentation. This helps to visualize how the components are located relative to each other and how the pores are distributed between them. Each of these compo-

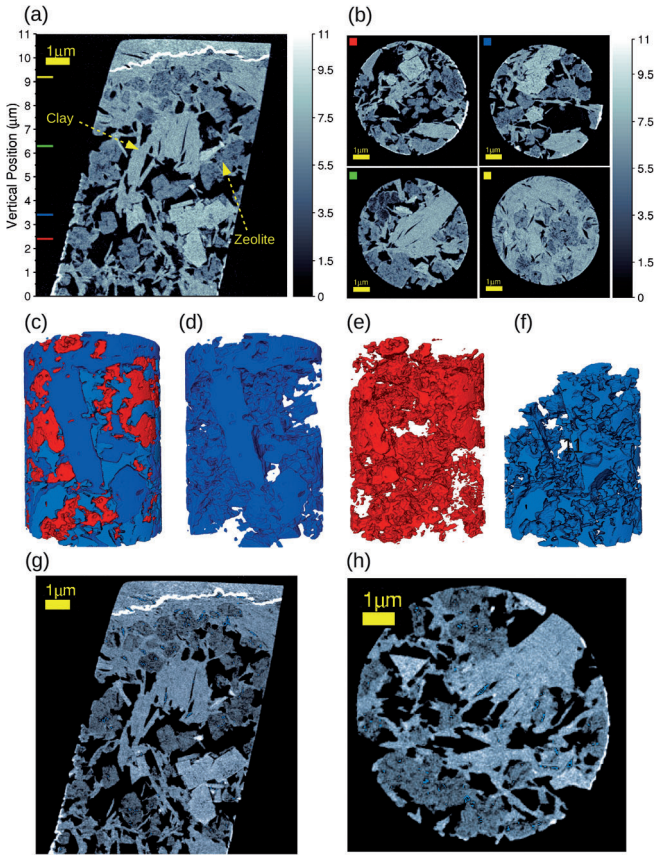

Figure 2. Ptychographic X-ray nanotomography results from the experiment with the FCC catalyst body. a) Vertical section from the middle of the electron-density tomogram. The 5% La_2O_3-exchanged zeolite type Y and metakaolin clay, identified based on their different electron density, are indicated. The vertical-position axis can be correlated to the one in Figure 3b. b) Some selected axial sections of the phase-contrast tomogram. The colored squares at the top-left corner correspond to the positions of the colored lines in (a). In (a) and (b), the gray intensity of the images is given in units of electron density ($\times 10^{23}$ electrons per cm^3). c) 3D rendering of the pores in light blue, the zeolite type Y in blue, and the metakaolin clay in red. (d–f) The renderings as in (c), but separated by component for better visualization of how the components are located to each other. g, h) Two orthogonal sections from the middle of the tomogram, some enclosed pores are shown in blue. Scale bars = 1 μm.

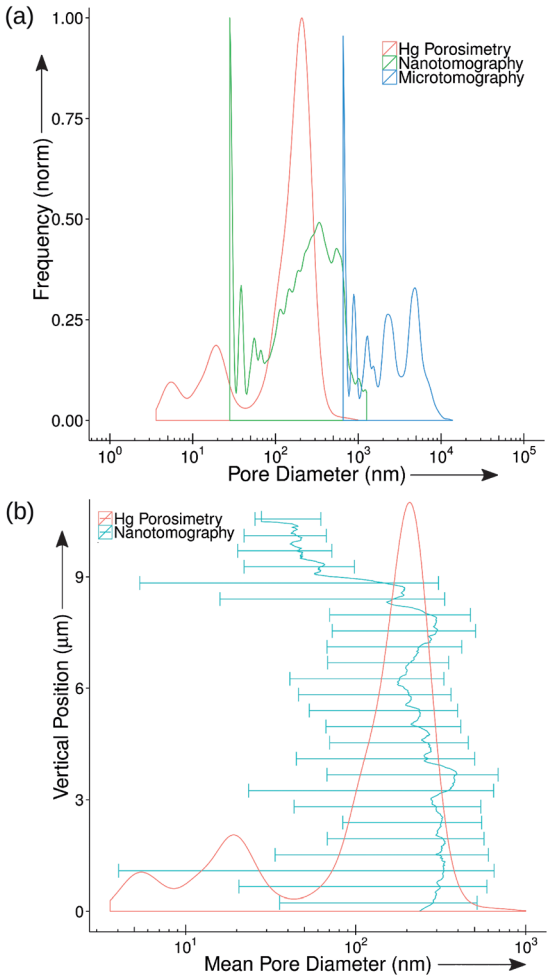

Figure 3. Pore-size analysis of FCC Catalyst body. a) Pore-size distributions (PSD) as a function of the pore diameter. The mercury PSD is shown in red. The pore-size distributions extracted from the 3D images obtained with X-ray imaging techniques are displayed in blue for the phase-contrast microtomography and in green for the ptychographic nanotomography. b) The variation of the mean value (solid line) and size-distribution range (bars) of the pore diameter plotted against vertical position calculated for 25 evenly divided bins of the tomogram from the bottom to the top. The vertical-position axis can be correlated to the one in Figure 2a. The mercury PSD is shown in red for reference.

nents is shown separately in Figure 2d–f, that is, the metakaolin clay (in blue), the zeolite (in red) and the pores (in light blue). A movie is available in the Supporting Information. We have also observed a few enclosed pores, in which the connectivity of pores larger than the image resolution (39 nm) was not noted. Some of them are displayed (in blue) in the two orthogonal slices in Figure 2g and Figure 2h.

Finally, the pore structure of this FCC catalyst body was assessed. The pore-size distributions (PSD) obtained by mercury porosimetry experiments and by image analysis of the X-ray imaging results are shown in Figure 3a. The former technique probed pores from approximately 3 to 1×10^3 nm, whereas the latter technique comprised two ranges. From the microtomography images, the pore diameters probed ranged from approximately 7×10^2 to 1×10^4 nm, which is a range that is approximately one order of magnitude higher than the mercury porosimetry results. From the nanotomography data, the pore diameters probed span a range of approximately 30 to 1.5×10^3 nm, which is in fairly good agreement with the range probed by mercury porosimetry, although the PSD shapes present some differences. These differences could be explained through the anisotropy. Although shape is easily quantified in the tomography data, it cannot be extracted from porosimetry measurements for comparison. The overlap between the results from the two X-ray imaging techniques indicate that ptychographic tomography can probe small pores (macropores between 50 and 1.5×10^3 nm and some mesopores between 39 and 50 nm) within the catalyst body structure, although the volume probed is small compared to the whole catalyst body. This can be complemented by microtomography, which can probe macropores larger than 700 nm in a larger and more representative volume. This covers a critical-length scale of pore sizes that is crucial for evaluating the catalyst performance. Notice in particular that the bottom values at the PSDs are limited by the resolution of the X-ray images. The dis-

crete nature of the image data creates sharp peaks at the beginning of each PSD corresponding to pores below the resolution limit as explained in the Supporting Information.

Beyond bulk porosity, the image analyses yield the 3D structure of the interparticle pore space and the padding of the catalyst components rather than only the pore-size distribution. This 3D structure can be used for further analysis and catalyst optimization by dynamic flow simulations. For example, Figure 3b shows the variation of the mean value and size-distribution range of pore diameters for each cross-section of the tomogram vertically from the bottom to the top. The vertical-position scale can be correlated to the one in Figure 2a. The mercury PSD is included for reference. Instead of a single ensemble distribution for the whole sample, it becomes apparent where bottlenecks and wide-pore regions are. For instance, such analysis reveals that the pore-size distribution at the top of the sample is shifted toward smaller pores as compared to the one at the bottom. We can also see that the zeolite and the clay are separated by interparticle pores of tens of nanometers, which enables large feed molecules to easily diffuse throughout the catalyst.

In summary, by combining X-ray imaging techniques that probe different length scales of the sample, the 3D structure of FCC preshaped catalyst bodies could be visualized. This enabled the visualization of padding of the different components of the catalyst bodies, which were 5% La_2O_3-exchanged zeolite type Y and metakaolin clay. We could visualize how these two components were separated by pores of tens of nanometers. In addition, the pore-size distribution could be obtained by analyzing the 3D structure of the interparticle pores within the catalyst body. The high resolution of 39 nm provided by ptychographic X-ray tomography allowed us to probe the pore diameters in a similar range as that probed by mercury porosimetry. This will open a new route for future simulations of flow dynamics through the sample, helping to better understand the molecule cracking locally during the FCC catalysis.

Experimental Section

For microtomography experiments, the catalyst bodies were added to a quartz capillary, and no further preparation was carried out. For the ptychographic X-ray nanotomography experiments, the sample was milled by using FIB to extract a cylinder of 8 μm diameter out of one spherical catalyst body with diameter of about 100 μm. This cylinder was mounted on the sample holder of the instrument.[21,22] Both X-ray imaging experiments were carried out at the Swiss Light Source, Paul Scherrer Institut, Switzerland. X-ray microtomography was performed at the TOMCAT beamline and ptychographic X-ray tomography was carried out at the cSAXS beamline. The mercury PSD measurement was carried out on a Micromeritics Autopore IV 9520 unit. Further experimental details and data processing are given in the Supporting Information.

Acknowledgements

We thank X. Donath for technical support at the cSAXS beamline, F. Arcadu (PSI) for the resolution estimation from the microtomography images, Dr. A. G. Bittermann (ScopeM, ETH Zürich) for the sample preparation with FIB microscope. We also thank the Swiss National Science Foundation (SNF) for the support to the work of J.C.d.S. (grant no. 137772). Instrumentation was supported by SNF (R'EQUIP, 145056, "OMNY") and the Competence Centre for Materials Science and Technology (CCMX) of the ETH-Board, Switzerland.

Keywords: nanostructures · porosity · ptychography · X-ray imaging · zeolites

[1] J. G. Speight, *The Chemistry and Technology of Petroleum*, 4th Ed., CRC Press, Taylor & Francis Group, Boca Raton, **2006**.
[2] J. Cejka, A. Corma, S. Zones, *Zeolites and Catalysis: Synthesis Reactions and Applications, Vol. 1*, Wiley-VCH, Weinheim, **2010**.
[3] K. S. W. Sing, D. H. Everett, R. A. W. Hall, L. Moscou, R. A. Pierotti, J. Rouquerol, T. Siemieniewska, *Pure Appl. Chem.* **1985**, *57*, 603–619.
[4] J. García-Martínez, K. Li, G. Krishnaiah, *Chem. Commun.* **2012**, *48*, 11841–11843.
[5] K. P. de Jong, J. Zecevic, H. Friedrich, P. E. de Jongh, M. Bulut, S. van Donk, R. Kenmogne, A. Finiels, V. Hulea, F. Fajula, *Angew. Chem. Int. Ed.* **2010**, *49*, 10074–10078; *Angew. Chem.* **2010**, *122*, 10272–10276.
[6] S. Brunauer, P. H. Emmett, E. Teller, *J. Am. Chem. Soc.* **1938**, *60*, 309–319.
[7] P. I. Ravikovitch, G. L. Haller, A. V. Neimark, *Adv. Colloid Interface Sci.* **1998**, *76–77*, 203–226.
[8] J. Landers, G. Y. Gor., A. V. Neimark, *Colloids Surf. A* **2013**, *437*, 3–32.
[9] A. J. Koster, U. Ziese, A. J. Verkleij, A. H. Janssen, K. P. de Jong, *J. Phys. Chem. B* **2000**, *104*, 9368–9370.
[10] A. H. Janssen, A. J. Koster, K. P. de Jong, *Angew. Chem. Int. Ed.* **2001**, *40*, 1102–1104; *Angew. Chem.* **2001**, *113*, 1136–1138.
[11] S. R. Bare, M. E. Charochak, S. D. Kelly, B. Lai, J. Wang, Y.-c. K. Chen-Wiegart, *ChemCatChem* **2014**, *6*, 1427–1437.
[12] J. Ruiz-Martínez, A. M. Beale, U. Deka, M. G. O'Brien, P. D. Quinn, J. F. W. Mosselmans, B. M. Weckhuysen, *Angew. Chem. Int. Ed.* **2013**, *52*, 5983–5987; *Angew. Chem.* **2013**, *125*, 6099–6103.
[13] C. A. Trujillo, U. Navarro-Uribe, P. P. Knops-Gerrits, L. A. Oviedo, P. A. Jacos, *J. Catal.* **1997**, *168*, 1–15.
[14] A. Snigirev, I. Snigireva, V. Kohn, S. Kuznetsov, I. Schelokov, *Rev. Sci. Instrum.* **1995**, *66*, 5486.
[15] D. Paganin, S. C. Mayo, T. E. Gureyev, P. R. Miller, S. W. Wilkins, *J. Microsc.* **2002**, *206*, 33–40.
[16] P. Cloetens, W. Ludwig, J. Baruchel, J.-P. Guigay, P. Pernot-Rejmánková, M. Salomé-Pateyron, M. Schlenker, J.-Y. Buffière, E. Maire, G. Peix, *J. Phys. D* **1999**, *32*, A145–A151.
[17] M. Dierolf, A. Menzel, P. Thibault, P. Schneider, C. M. Kewish, R. Wepf, O. Bunk, F. Pfeiffer, *Nature* **2010**, *467*, 436–439.
[18] M. Guizar-Sicairos, A. Diaz, M. Holler, M. S. Lucas, A. Menzel, R. A. Wepf, O. Bunk, *Opt. Express* **2011**, *19*, 21345–21357.
[19] A. Diaz, P. Trtik, M. Guizar-Sicairos, A. Menzel, P. Thibault, O. Bunk, *Phys. Rev. B* **2012**, *85*, 020104.
[20] H. M. L. Faulkner, J. M. Rodenburg, *Phys. Rev. Lett.* **2004**, *93*, 023903.
[21] M. Holler, J. Raabe, A. Diaz, M. Guizar-Sicairos, C. Quitmann, A. Menzel, O. Bunk, *Rev. Sci. Instrum.* **2012**, *83*, 073703.
[22] M. Holler, A. Diaz, M. Guizar-Sicairos, P. Karvinen, E. Färm, E. Härkönen, M. Ritala, A. Menzel, J. Raabe, O. Bunk, *Sci. Rep.* **2014**, *4*, 3857.
[23] P. Thibault, M. Dierolf, A. Menzel, O. Bunk, C. David, F. Pfeiffer, *Science* **2008**, *321*, 379–382.
[24] M. Guizar-Sicairos, J. R. Fienup, *Opt. Express* **2008**, *16*, 7264–7278.
[25] P. Thibault, M. Guizar-Sicairos, *New J. Phys.* **2012**, *14*, 063004.
[26] A. Guinier, *X-Ray Diffraction In Crystals, Imperfect Crystals, and Amorphous Bodies*, Dover Publications Inc., New York, **1994**.
[27] A. Diaz, M. Guizar-Sicairos, A. Poeppel, A. Menzel, O. Bunk, *Carbon* **2014**, *67*, 98–103.
[28] M. Langer, A. Pacureanu, H. Suhonen, Q. Grimal, P. Cloetens, F. Peyrin, *PLoS ONE* **2012**, *7*, e35691.

Received: November 19, 2014
Published online on December 17, 2014

